ASME Journal of Engineering for Gas Turbines and Power
Online journal at:
https://asmedigitalcollection.asme.org/gasturbinespower

Aggelos Gaitanis[1]
Institute of Mechanics, Materials and Civil Engineering (iMMC),
Université Catholique de Louvain,
University of Mons (UMONS),
Louvain la Neuve 1348, Belgium
e-mail: angelos.gaitanis@uclouvian.be

Ravi Nath Tiwari
Thermochemical Power Group (TPG),
University of Genoa,
Genoa 16145, Italy

Ward De Paepe
Thermal Engineering and Combustion Unit,
University of Mons (UMONS),
Mons 7000, Belgium

Mario Luigi Ferrari
Thermochemical Power Group (TPG),
University of Genoa,
Genoa 16145, Italy

Francesco Contino
Institute of Mechanics, Materials and Civil Engineering (iMMC),
Université Catholique de Louvain,
Louvain la Neuve 1348, Belgium

Peter Breuhaus
Norwegian Research Centre AS (NORCE),
Stavanger 4021, Norway

Operational Strategies of Two-Spool Micro Gas Turbine With Alternative Fuels: A Performance Assessment

Micro gas turbines (mGT) have not yet succeeded in conquering the small-scale combined heat and power (CHP) market. One reason is that their electrical efficiency is not high enough to maintain a cost-effective operation. A two-shaft intercooled mGT has the potential to meet the current market demand. This technology maintains a high electrical efficiency even at part-load and coupled with its fuel-flexible combustion chamber, it is an ideal candidate for CHP concepts in a renewable future. In this paper, performance analysis on two-spool mGT is carried out with various fuel blends. Attention is given to the low-pressure and high-pressure compressors and the variation of surge margin by adding hydrogen and syngas. Two control strategies for the mGT are adopted. In the first scenario, the two shafts have equal rotational speeds while in the second, the speeds are controlled independently. As the engine is operated at equal speeds, the maximum performance with 100 vol. % of syngas is observed at 85% of the nominal load while 100 vol. % of hydrogen shows maximum efficiency at a load of 63.7%. At electric power lower than 60% and for high amounts of syngas in natural gas, the low-pressure compressor (LPC) operates closely to surge line. In the second scenario, the efficiency increases as the load decreases and the LPC runs in an efficient and safe operating region. Additionally, the amount of nitrogen in syngas affects the part-load performance of the two-spool mGT. [DOI: 10.1115/1.4064798]

Introduction

Renewable energy systems are being discussed globally, which has led to an increase in the use of low-emission energy resources. If low-emission technologies and renewable fuels are not introduced promptly and the electricity production continues to grow rapidly, a significant increase in greenhouse gas emissions will be observed in the coming decades. Decentralized and hybrid power systems present many benefits (i.e., improving overall efficiency and minimizing emissions) [1] in future power production. In that context, micro gas turbines (mGT) could play an important role in such systems, but their low efficiency and high specific price per kilowatt prevent them from being implemented effectively. Micro gas turbines power capacities are not well defined but are generally specified between 10 kW and 500 kW [2]. The typical performance of such an engine is lower than that of their competitor in the market (i.e., internal combustion engines—ICE).

Historically, microturbine technology has been researched since 1970, when the automotive industry began to consider replacing reciprocating piston engines [2,3]. Microturbines have not had great success in the automotive sector as they show lower transient response and higher cost compared to ICE [2]. However, they could play an imperative role in developing decentralized and hybrid energy systems in the current era. By increasing their performance coupled with state-of-the-art technologies and using renewable fuels, they could meet market demand in terms of emissions and efficiency.

Micro gas turbines are considered to be promising technologies due to their fuel flexibility, low emissions, high power density, and low maintenance costs [4,5]. Despite their relatively low exhaust temperatures (around 150–300 °C), their waste heat can still be utilized to generate low-pressure steam and/or hot water [2]. The heat provided by mGT exhaust allows it to be implemented in

Turbomachinery Technical Conference & Exposition, Hynes Convention Center, June 26–30, 2023. Turbo Expo 2023.
[1]Corresponding author.
Manuscript received October 25, 2023; final manuscript received January 11, 2024; published online March 20, 2024. Editor: Jerzy T. Sawicki.

combined cycle concepts [6]. The thermal recovery performed by the organic Rankine cycle (ORC) bottomed to an mGT can increase the combined cycle thermal efficiency by 15% [7]. Also, concepts like the micro humid air turbine (mHAT) [8] proved to increase the performance of the engine significantly. Moreover, bladeless or Tesla technology can play a vital role in increasing the compressor's performance due to its reversible operation, low manufacturing costs, and low noise [9]. In that context, an alternative mGT concept, which is the two-spool intercooled mGT, was introduced. This engine seems capable of successfully conquering the small-scale combined heat and power (CHP) market. This two-spool intercooled mGT presents an electrical efficiency of around 40% and is capable of incorporating a range of fuels [10]. In the literature, two studies can be found that describe the design of this engine [11,12], where especially Malkamäki et al. have indicated that its efficiency and cost can be compared with a reciprocating engine from MWM GmbH of the same load [11].

Besides increasing the efficiency of decentralized production, the world also focuses on renewable fuels, such as hydrogen, syngas, and biogas [1,13], in response to the growing demand for low-emission technologies. The shift towards more renewable energy production also pushes the mGT to become more flexible in terms of fuel utilization. Therefore, apart from natural gas, alternative fuels with lower energy content, like syngas and biogas should be used. Moreover, the energy transition requires the utilization of hydrogen as the main fuel. Given the occasionally limited availability of these fuels, the mGT should thus be capable of running on both classical fossil-based gaseous fuels, hydrogen which has a high lower heating value (LHV), and alternative fuels like syngas which have a rather low LHV. The addition of alternative fuels could restrict the mGT operation as compressor surge can occur due to the decreasing air mass flow rate. Also, the combustion process when natural gas is mixed with syngas or hydrogen can cause combustion instabilities, leading to flameout (syngas) or flashback (hydrogen).

Having that in mind, researchers [14–17] studied the impact of using hydrogen and/or a blend of natural gas/hydrogen on the mGT both numerically and experimentally. Hydrogen addition in methane increased the flame temperatures, with cooling and NO_x emissions being the primary concerns [14,15]. Also, an experimental and numerical study on a pure hydrogen-fueled gas turbine highlighted the higher outlet velocity and pressure drop in the combustion chamber (CC) compared to pure natural gas operation [16]. Pappa et al. showed that the reactivity of hydrogen can be lower by applying steam as a diluent using large eddy simulation [17].

Similarly, different combustion challenges are observed when syngas is used instead of hydrogen. Bompas et al. [18] numerically compared carbon monoxide levels when using natural gas or syngas, indicating that syngas does not significantly impact combustion efficiency. Diaz et al. [19] examined the energy and exergy efficiencies of a syngas mGT cogeneration system while also analyzing the total costs associated with the production of energy from syngas obtained by gasification. They showed that increasing the compression ratio improves the thermodynamic performance, but the cost of the system per unit of time is increased as well. Furthermore, it was found that the CC presented the highest rate of exergy destruction [19]. Thermodynamic and computational fluid dynamics (CFD) analyses have been performed on a small-scale integrated energy system composed of mGT-ORC-gasifier focusing on the performances of five different syngas-biogas fuels. This study indicated the necessity of operating the mGT in particular conditions, as determined by the compressor and turbine performance maps of the AE-T100 due to the low LHV of the fuels [20]. Renzi et al. assessed numerically the behavior of the same mGT cycle when it is fed with biomass-derived syngas showing that the use of syngas decreased the overall efficiency of the system by 5% due to the higher thermal input that is required to keep the produced power at the nominal value [21]. They also included a steam injection gas turbine (STIG) cycle to counteract the negative effects of syngas utilization on the cycle performance. De Paepe et al. extended the work of Renzi et al. by comparing two steady-state models and validating them in their capability to simulate steam injection in the T100 mGT fed with natural gas and syngas [22]. When the cycle runs with syngas some variation in performance parameters between both models is observed, which confirms the importance of the accurate and extensive modeling of the combustion chamber [22].

The above-mentioned studies analyze the performance characteristics of running mGT engines with alternative fuels. Numerical and experimental works studied the exhaust gas emissions and the required design modifications of CC to incorporate syngas or hydrogen. Although extensive performance analysis on one of the most promising mGT (i.e., two-spool mGT) in the market by utilizing several alternative fuel mixtures is still missing in the literature. The purpose of this article is thus to study the performance of a two-spool mGT from a thermodynamic point of view when applying various fuel mixtures, including natural gas (NG), syngas (SG), and hydrogen (H_2). For this analysis, a steady-state model of the two-spool engine was developed in Python programming language and the combustion mechanisms were embedded according to GRI-MECH 3.0 library. As validation, the 0D model is compared with another model of the two-spool mGT from the literature. Additionally, two part-load strategies are employed for the steady-state modeling of this cycle to simulate the part-load behavior. These strategies are compared regarding the electrical efficiency (η_{el}) and the behavior of both compressors. The structure of this paper is as follows: In the Methodology section, the numerical model is described thoroughly, and the two part-load strategies regarding the operation of the cycle are presented. In the Results section, the behavior of several fuel mixtures is discussed at nominal and part-load levels. Finally, the Conclusions section includes the outcomes of this study and the future perspectives of our work.

Methodology

In this section, the mGT (two-spool engine) used for the numerical model is presented. Then, the description of the modeling techniques that are adopted for this analysis, along with the two part-load strategies, are presented.

Two-Spool Intercooled Micro Gas Turbines. The basis of this numerical model is a two-spool mGT, which has similar performance characteristics as the Aurelia A400 mGT [10]. This engine is a recuperated Brayton cycle and consists of two shafts, as shown in Fig. 1. The low-pressure compressor (LPC), low-pressure generator, and low-pressure turbine (LPT) are mounted on the low-pressure shaft (LPS). Additionally, the high-pressure compressor (HPC), high-pressure generator, and high-pressure turbine (HPT) are part of the high-pressure shaft (HPS). The recuperator uses the exhaust gases to increase the enthalpy of the working fluid before it enters the combustion chamber (CC) (5). The other heat exchanger (i.e., the intercooler) cools down the air at the HPC inlet (3) to increase the component's isentropic efficiency. The electrical power is generated from the two high-speed power generators and the power electronics needed to convert the two produced powers to grid frequency. This cycle can achieve an electrical efficiency higher than 40% for a nominal power of 400 kW [10]. The typical specifications of this engine are shown in Table 1. The two-spool machine operates at constant power and behaves similarly to a single-spool variable-speed mGT. Such machines allow the operator to keep the turbine inlet temperature (TIT) constant at high levels while reducing the rotational speed to operate at part load while still maintaining high electrical efficiency. In this specific engine, however, the two shafts can be controlled independently of each other. This allows the turbomachinery components to run at high efficiency for a larger operating range than with a single-shaft engine. Therefore, as the demanded power is decreased, the rotational speeds are decreased and TIT is kept constant by the controller. When the maximum allowable turbine exhaust temperature (TET) is reached at 40% load, the TIT is starting to reduce as well. Then, the electrical efficiency of the engine experiences a sharp

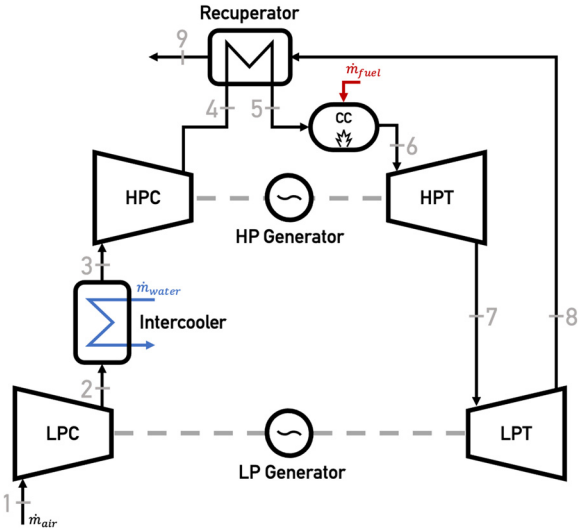

Fig. 1 The two-spool mGT is a two-shaft recuperated Brayton cycle with an intercooler between the low-pressure and high-pressure compressors. The intercooler decreases the temperature at point 3 to increase the air density and efficiency of the high-pressure compressor. The recuperator preheats the air coming from the compressor with the exhaust hot gases.

Table 1 The nominal specifications of Aurelia A400 given by the manufacturer [10]

Nominal electric power, $P_{e,\text{nom}}$	400 kW_e
Nominal electrical efficiency, $\eta_{\text{el,nom}}$	40.2%
Exhaust gas flow at full power	2.2 kg/s
Exhaust gas temperature at full power	185 °C

decrease, as presented by Jaatinen-Värri et al. [23] with the cooperation of Aurelia Turbines Oy [10].

Numerical Model. In this section, the in-house numerical model developed to study the impact of fuel alteration on the performance of a two-spool mGT is extensively described. This software can predict the nominal and part-load behavior of a two-spool mGT by using two different part-load schemes.

The modeling methods that are applied to each component of the mGT cycle are similar to a previous study from part of the authors [24]. In this study, the results of the transient T100 mGT were validated in steady-state and transient conditions. For the current study due to the lack of experimental results and data from the manufacturer (Aurelia Turbines Oy, Lappeenranta, Finland), our model adopted the design, boundary and initial conditions from the available studies on the Aurelia A400. After the description of the modeling methods, the complete model is compared with another study from the literature [11] and with the design specifications of Aurelia A400 [10] to confirm the accurately developed methodology (see later).

The fluid properties are modeled using different equations of state from the Coolprop library [25]. For example, the fluid behavior of water is calculated with IAPWS (International Association for the Properties of Water and Steam) 1995 [26]. The great advantage of this library is the representation of real gas behavior compared to most equations of state that emanate from the assumption of ideal gas behavior using reference states.

The compressor maps are extracted from literature [12] and digitized to calculate the pressure ratio and isentropic efficiency of the LPC and HPC. Figure 2 presents the LPC and HPC maps. The values are normalized using the design (des) parameters of the maps. The design parameters correspond to the compressors' nominal conditions at 400 kW_e and are shown in Table 2. These values were extracted for Malkamäki et al. [11] and are used to calculate the normalized pressure ratio, isentropic efficiency, reduced (red) shaft speeds ($N_{\text{red}} = N/\sqrt{T_{\text{in}}}$) and mass flowrate ($\dot{m}_{\text{red}} = \dot{m}\sqrt{T_{\text{in}}}/p_{\text{in}}$) from the two compressors. The rotational speeds of the LPS and HPS are equal at nominal conditions, so the design shaft speed is 33,200 rpm for both compressors. The model applied the same fitting techniques that were presented in a previous study [24] for both compressors using a Supershape fitting equation for the pressure ratio and an Ellipse equation for the efficiency. As a result, the pressure ratio and the isentropic efficiency are calculated using the mass flowrate and the rotational speed as inputs for each component (LPC, HPC). The outlet enthalpy of the compressor components is calculated using the isentropic efficiency ($\eta_{is,c}$) as in the following equation:

$$h_{\text{out}} = h_{\text{in}} + \frac{h_{\text{out,is}} - h_{\text{in}}}{\eta_{\text{is,c}}} \tag{1}$$

where h_{in} is the specific enthalpy of air at the inlet of each compressor, $h_{\text{out,is}}$ is the specific enthalpy at constant specific entropy ($s_{\text{in}} = s_{\text{out}}$). The outlet temperature is given using the fsolve function from the SciPy library [27]. Therefore, for a given fluid composition and specific enthalpy, this algorithm finds the temperature when $h(T_{\text{out}}) - h_{\text{out}} = 0$. Moreover, the compressor surge margin which is a useful value to determine whether the component experiences flow instabilities, is calculated as presented below:

$$\text{SM} = \left.\frac{\dot{m}_c - \dot{m}_{c,\text{sl}}}{\dot{m}_c}\right|_{N=\text{const}} \times 100\% \tag{2}$$

where $\dot{m}_{c,\text{sl}}$ is the mass flowrate at the surge line considering constant rotational speed.

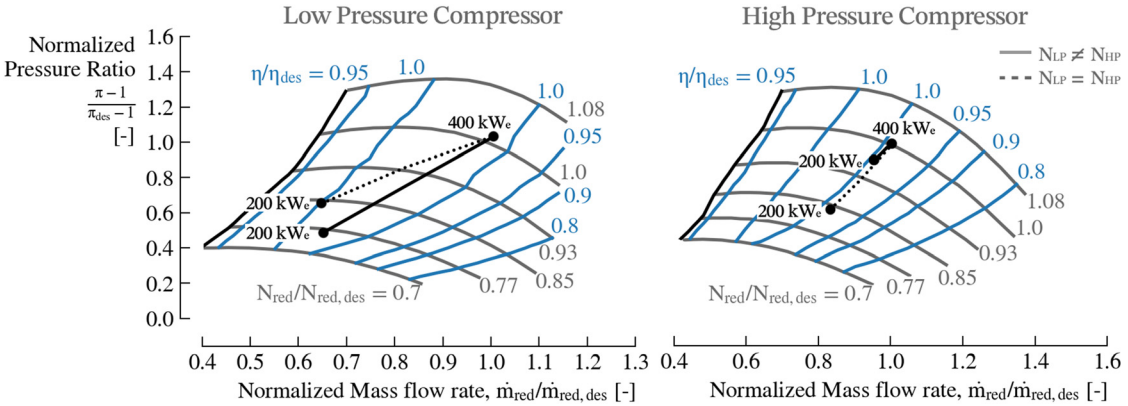

Fig. 2 Compressor performance maps generated by digitization of the data presented by Jaatinen-Värri et al. [12]. The evolution of the operating point, depending on the control strategy in both maps is presented.

Table 2 The design compressor parameters are calculated by Malkamäki et al. [10] and are the nominal conditions of the two compressors

Design rotational speed, N_{des}	33,200 rpm
Design mass flow rate, $\dot{m}_{air,des}$	2.085 kg/s
Design LPC pressure ratio, $\pi_{LPC,des}$	2.7
Design HPC pressure ratio, $\pi_{HPC,des}$	1.846
Design LPC isentropic efficiency, $\eta_{LPC,des}$	0.8
Design HPC isentropic efficiency, $\eta_{HPC,des}$	0.82
Design LPT, HPT isentropic efficiency, $\eta_{T,des}$	0.84

The HPT is considered choked in the simulations. This assumption is adopted due to the lack of any information regarding the turbine performance maps and it is considered a standard practice in gas turbine modeling. As a result, the maximum amount of mass flowrate through the HPT is fixed by the choking constant, which is presented as [28] (Eq. (3))

$$K_c = \frac{\dot{m}_{HPT}\sqrt{TIT}}{p_{in,HPT}} = A\sqrt{\frac{k_{HPT}}{R}\left(\frac{2}{k_{HPT}+1}\right)^{\frac{k_{HPT}+1}{k_{HPT}-1}}} = const \tag{3}$$

where $p_{in,HPT}$ is the pressure at the inlet of the turbine, k_{HPT} is the average heat capacity ratio of the gas at the HPT, R corresponds to the gas constant and A is the cross-sectional area of the turbine. First of all, the cross-sectional area is calculated by running the simulation at nominal conditions and knowing the $\dot{m}_{HPT}$, TIT, and $p_{in,HPT}$. Then this value is used to calculate the choke constant. Introducing different fuel properties in the cycle, the k_{HPT} changes, depending on the heat capacity of the gases in the outlet of CC. The initial isentropic efficiency in both turbines is assumed to have the value that is shown in Table 2. Similarly, the influence of k on the initial isentropic efficiency of the HPT and LPT is addressed as the gas properties change. This is done, as suggested by Parente et al. [29], with the following equation:

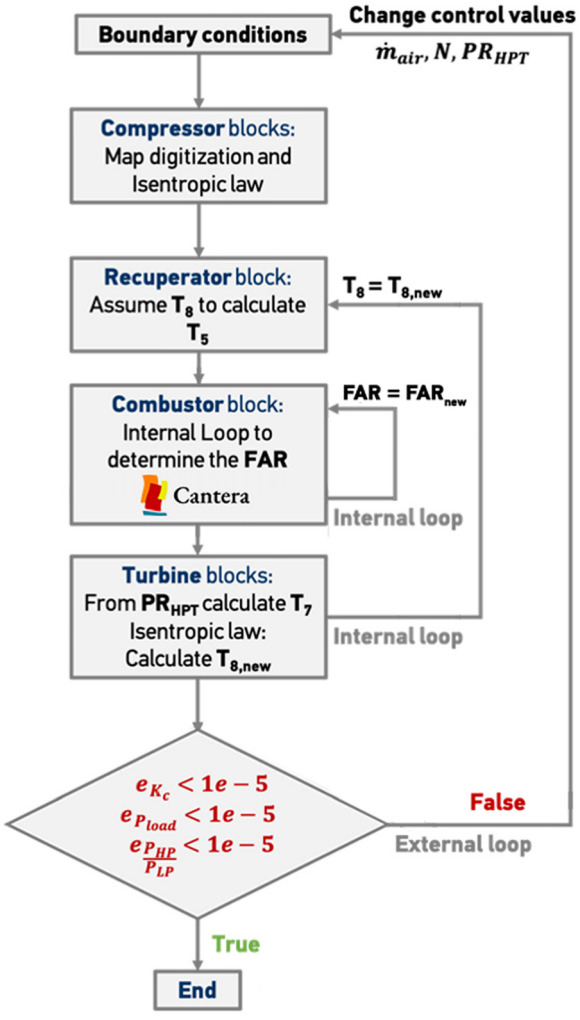

Fig. 3 Flow chart of the calculation steps of the two-spool mGT 0D model. Three control parameters are used to keep the choke constant, electric power, and power ratio at specific values.

$$\frac{\eta_{is}}{\eta_{is}^*} = \frac{k-1}{k^*-1}\sqrt{\frac{k^*+1}{k+1}\frac{1-1/\pi^{(k^*-1)/k^*}}{1-1/\pi^{(k-1)/k}}} \tag{4}$$

where the asterisk (*) refers to the properties of standard dry air and π to the pressure ratio of the component. This equation was proposed by Parente et al. [29] for humidified mGTs but can also be applied for fuel alterations. The HPT pressure ratio is an input and a control variable in this model, while the LPT pressure ratio is calculated by assessing the pressure losses in the recuperator hot side to find p_8 (see Fig. 1). The HPT and LPT outlet temperatures are calculated the same way as the outlet temperature of the compressors using fsolve. The outlet-specific enthalpy is derived from the following equation:

$$h_{out} = h_{in} - \eta_{is,T}(h_{in} - h_{out,is}) \tag{5}$$

Regarding the heat exchanger modeling, a correlation was made for the recuperator effectiveness (ϵ_{rec}) based on the information from Jaatinen-Värri et al. [23]. Therefore, the effectiveness is a function of the mass flowrate at the cold side inlet (point 4). A constant value was adopted for the intercooler effectiveness (ϵ_{int}) due to the limited information regarding this component. As a result, the effectiveness is assumed to be 0.9155 to match the HPC inlet temperature presented by Jaatinen-Värri et al. [12] at nominal conditions. The temperature at the outlet of the intercooler hot side (point 3) and recuperator cold side (point 5) is given by the equations below:

$$T_5 = T_4 + \epsilon_{rec}(T_8 - T_4) \tag{6}$$

$$T_3 = T_2 - \epsilon_{int}(T_2 - T_{w,in}) \tag{7}$$

where $T_{w,in}$ is the inlet temperature of the water at the cold side of the intercooler and it is kept at 15 $^\circ C$ during the simulations. The cold side of the intercooler utilizes water with a sufficient mass flowrate of 2.1 kg/s. The numbering of Eqs. (6) and (7) corresponds to the different states shown in Fig. 1.

At the CC outlet, the temperature (TIT) is kept constant and equal to 977 $^\circ C$. This temperature is considered acceptable for the materials of the HPT and corresponds to the information derived from a company associated with Aurelia Turbines [30]. The gas properties after the combustion process are calculated with the object-oriented CANTERA software [31] using the GRI-MECH 3.0 library. The code uses the method "equilibrate" object which invokes CANTERA's chemical equilibrium solver and uses an element potential method. The element potential method is one of a class of equivalent nonstoichiometric methods that solves a set of N nonlinear algebraic equations, where N is the number of elements (not species). The gas properties are determined by knowing the fuel-to-air ratio (FAR), the TIT, and the thermodynamic properties at point 5 (Fig. 1). Therefore, an initial value for the FAR is assumed and the new FAR is determined by solving the energy balance (Eq. (8)) of CC with an iterative method

$$FAR_{new} = \frac{(FAR+1)h_6 - h_5}{LHV \cdot \eta_{cc}} \tag{8}$$

η_{cc} corresponds to the combustion efficiency of CC and is 0.99. Also, the pressure losses at CC are taken into account as equal to 3%.

The power ratio (P_eR) between the generated power of HPS and LPS is extracted from the literature and has a value of 1.1473 [23].

This power ratio is considered when the LPS and HPS have the same rotational speed at nominal load. The two generators have 96% electromechanical efficiency and the efficiency of the inverter is 98%.

The complete steady-state model of the cycle operating with dry air is presented in Fig. 3. The model uses an iterative method that starts at the inlet of the cold side of the recuperator to accurately calculate the inlet hot side temperature T_8. We assume a value of T_8 to calculate the T_5 in the recuperator block and then determine the thermodynamic values in the inlet and outlet of CC and Turbine blocks until the error of T_8 between iterations is below 10^{-5}. The external iteration essentially controls the mGT cycle. The simulation converges by changing three user-defined constant values using the Secant method. Therefore, $\dot{m}_{\text{air}}$ controls K_c, $N = N_{\text{LP}} = N_{\text{HP}}$ controls the electrical power (P_e) and PR_{HPT} controls $P_eR = P_{\text{HP}}/P_{\text{LP}}$.

Part-Load Management. Two different part load control schemes are employed. The first scenario (case 1) considers the LPS and HPS to run at equal rotational speeds. This control scheme allows us to use only the N_{LP} as a value that adjusts the produced electric power. As a result, the unknown parameters of the system are only the 3 control variables that enable the model to converge. In the second scenario (case 2), N_{LP} and N_{HP} operate at different rotational speeds. The LPS rotational speed is the control value that determines the produced power like in case 1, but the HPS rotational speed is a function of the electric power according to the following equation:

$$N_{\text{HP}} = f_{\text{NR}}(P_e) \cdot N_{\text{LP}} \tag{9}$$

where the shaft speeds ratio (NR) is the ratio between the high pressure (HP) and low pressure (LP) speeds and is a function of the electric output. The correlation between the generated power and the HPS rotational speed is derived from a study on the control strategies of Aurelia A400 [23]. Also, the power ratio (P_eR) should be a function of the produced electric power ($P_eR = f(P_e)/P_{e,\text{nom}}$) as the two shafts are not loaded equally. Both correlations are made with a linear interpolation between the input values. Thus, by applying these two correlations to case 2, it is possible to utilize the part-load control scheme that is suggested by the Aurelia A400 studies in the literature [12,23]. Figure 2 shows the operating lines of case 1 ($N_{\text{LP}} = N_{\text{HP}}$, dashed line) and case 2 ($N_{\text{LP}} \neq N_{\text{HP}}$, solid line) in both high-pressure and low-pressure compressor maps. The LPC operating line of case 2 is observed in the high-efficiency region as shown in Fig. 2. Whereas in case 1, the reduction in pressure ratio at part-load is less compared to the nominal point. Also, case 1 presents lower efficiencies for the same mass flow rate. The HPC operating line of case 2 shows higher pressure ratios than case 1 to compensate for the behavior of the LPC operating line. As a result, case 2 HPC operates in a small pressure ratio and shaft speed region compared to case 1.

Figure 4 depicts the electrical efficiency behavior at part load until 200 kW_e in both cases. As it is shown, case 2 presents slightly higher efficiency over the whole operating range. However, the efficiency difference is rather small and less than 1% even in 50% of the nominal load. Moreover, the efficiency increases as the generated electric power drops. On the other hand, in case 1, the efficiency starts to drop after 280 kW. Also, no significant difference in efficiencies is observed from 400 to 350 kW.

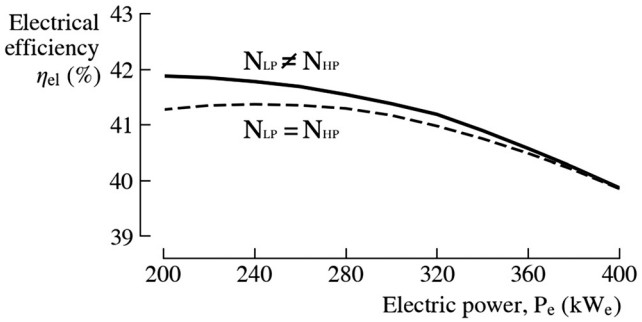

Fig. 4 Electrical efficiency behavior from 200 to 400 kW versus the produced electric power at two different control schemes (case 1: $N_{\text{LP}} = N_{\text{HP}}$, case 2: $N_{\text{LP}} \neq N_{\text{HP}}$). The two part-load management methods do not show significant divergence in efficiency. At half the nominal load, case 2 presents a higher efficiency of less than absolute 1% than case 1.

Model Comparison. The developed 0D model is compared to a model presented in literature about the Aurelia A400 prototype [12]. For this comparison, the model should operate with the same parameters that have been described above (Tables 1 and 2) except for the TIT and $T_{w,\text{in}}$ to match the operating conditions of the study [12]. Therefore, the TIT is kept at 1077 °C, $T_{w,\text{in}}$= 5 °C and the produced power is set at 455 kW_e, as this was the power reported on the specific work of the prototype. However, this power output is only used for the comparison of the two models. After the verification of our model, we will use the characteristics of the commercialized version, meaning that we limit our analysis to 400 kW_e. Figure 5 presents the relative error of temperature and pressure at points 2, 3, 4, 5, 7, and 8 (see Fig. 1). The relative error is calculated with the following expression (Eq. (10)):

$$e = \frac{|x_p - x|}{x_p} \times 100\% \tag{10}$$

where the values of our model are shown as x and the values of the study [12] as x_p.

The values of temperature and pressure present an error below 0.7% which confirms the accurate use of the component methods that were applied for this study (Fig. 5). Also, the relative error of the electrical efficiency is 5.96%, as the electrical efficiency of the study [12] and the one we calculated are 45.8% and 43.07% respectively. The increased error in electrical efficiency could be associated with the fact that our simulation model does not use the turbine performance maps to calculate the operating parameters (pressure

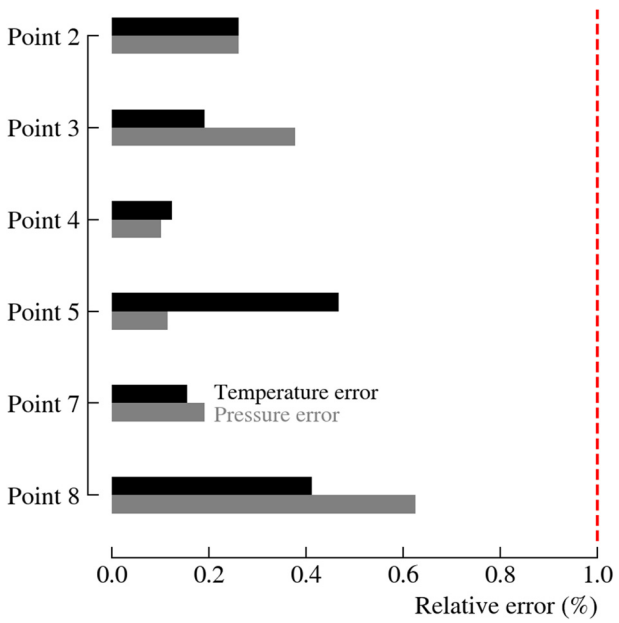

Fig. 5 Relative error for the steady-state comparison of our model and the model of Jaatinen-Värri et al. [12] at operating load of 455 kW_e. The error is below 0.7% for the values of pressure and temperature.

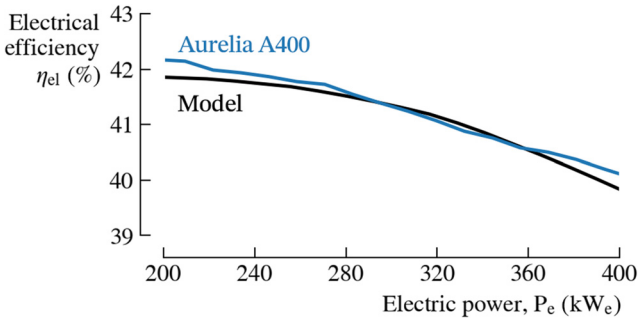

Fig. 6 Steady-state results of electrical efficiency (black line) at an electric power range of 200–400 kW_e compared with the electrical efficiency presented in the Aurelia Turbines Oy datasheet [10] (Aurelia A400 line). The part-load relative error does not exceed 0.75% which is sufficient.

ratio and shaft speed) of HPT and LPT. Moreover, the study [12] has no information regarding the LHV of natural gas in this publication.

The part-load performance of the model is compared with the only available data regarding the Aurelia A400 in the literature. Therefore, the partial load efficiency of this machine was extracted with digitization from the Aurelia Turbines Oy datasheet [10]. This data is depicted with a blue line in Fig. 6. In this part-load comparison, the model runs with a TIT of 977 °C and $T_{w,in} = 5$ °C as suggested by Ref. [30] for each produced power that is set. As a result, the operating conditions of this comparison differ from the comparison that is conducted in Fig. 5. The results of Fig. 6 show that the efficiency relative error between the Aurelia Turbines Oy datasheet and the model is below 0.75%. The highest error is 0.742% and is observed at 200 kW_e. Also, the results of the model follow adequately the efficiency data and have a similar trend. Thus, both comparisons confirm the accuracy of our modeling methods and allow us to utilize this code to carry out a performance assessment in this study.

Fuel Consideration. In this section, the fuels that are used for this analysis are described. First, the compositions of syngas should be chosen with care as the volume percentage of hydrogen (H_2) and carbon monoxide (CO) influence dramatically the LHV of the fuel and the combustion characteristics in general.

Syngas can be produced in several ways, while hydrogen percentages vary depending on the quality of the fuel input. Wood chips should have a moisture content of 20% to produce the maximum amount of hydrogen and lower tar. The presence of hydrogen in syngas generated by wood ranges between 5% and 30% based on literature data [32–35]. For this study, we considered an average amount of moisture in the wood chips. As a result, the amount of H_2 is 15.46% as shown in Table 3. Moreover, NG is composed mainly of methane with a percentage of 91.2% with the ethane and propane amounts being lower than 10%. Table 3 shows that the LHV of syngas is 47% of the LHV of natural gas. This difference in the stored energy of these two fuels could significantly alter the engine's operating conditions. The third fuel that we use for the testing of different mixtures in the two-spool mGT cycle is pure hydrogen with a 119.90 MJ/kg lower heating value.

Table 3 NG, SG compositions, and LHV

	Compositions (vol. %)							LHV
	CH_4	C_2H_6	C_3H_8	CO	CO_2	N_2	H_2	(MJ/kg)
NG	91.2	6.7	2.1	–	–	–	–	49.78
SG	3.05	–	–	31.46	5.03	45	15.46	23.41
H_2	–	–	–	–	–	–	100	119.90

Results and Discussion

In this section, the numerical results of the model using different fuel mixtures composed of NG, SG, and hydrogen (H_2) are presented. The steady-state model applied two different control schemes for the part-load operation and the results are depicted as well. In the control scheme of case 1, the rotational speeds of LPS and HPS have the same value at part-load. Whereas, in case 2 the shaft speeds are not equal except for the nominal conditions. Thus, the solid-line curves, in the figures below, refer to simulations performed using the control scheme of case 2 ($N_{LP} \neq N_{HP}$) and the dashed lines belong to case 1 ($N_{LP} = N_{HP}$).

For the first step of the analysis, we increased the amount of hydrogen and syngas in a blend with natural gas at three different operating points. So, the electrical efficiency, at a generated electric power of 400, 300, and 200 kW, is calculated by varying the syngas and hydrogen content of the fuel from 0 vol. % to 100 vol. % with 10 vol. % increments. Second, we present the behavior of different fuel mixtures of syngas and hydrogen at a generated power range of 200 to 400 kW with a power step of 10 kW. The electrical efficiency is calculated as (Eq. (11))

$$\eta_{el} = \frac{P_e}{\dot{m}_f \text{LHV}} \tag{11}$$

$\dot{m}_f$ is the fuel flow rate that is injected in the cycle.

Fuel Variation at Constant Power. As the volume percentage of hydrogen is increased in natural gas from 0% to 100%, the LHV of the fuel mixture increases significantly. This will lead to a decrease in the fuel flow rate. With pure natural gas as baseload, the fuel flow rate is 20.2 g/s, and with pure hydrogen 8.34 g/s. This results in a 58.2% fuel flow decrease. Due to the increased water content of the flue gases, the density and specific heat capacity at point 6 increase. This change in heat capacity of 1.32% leads to a slight drop in the air mass flowrate of 1.41%. All these minor changes, in the conditions of the engine at pure hydrogen, move the operating point of the LPC and HPC in the performance map approximately 0.1% toward the surge limit. This divergence in the operating conditions is very small and the change in electrical efficiency is below 0.2% not only at nominal but also at part-load for both control schemes (cases 1 and 2).

Although we do not see any significant performance alteration when we increase the amount of hydrogen in the fuel, syngas presents a major impact. The amount of syngas in natural gas is increased from 0 to 100 vol. % at 200, 300, and 400 kW of electric load with a 10 vol. % step. The results of electrical efficiency are shown in Fig. 7. We observe that at nominal load ("$P_e = 400$ kW_e" line) the performance of the cycle remains somewhat constant around 39.88%. Only from 90 to 100 vol. %, the efficiency is slightly decreased. When applying the operational strategy of case 1

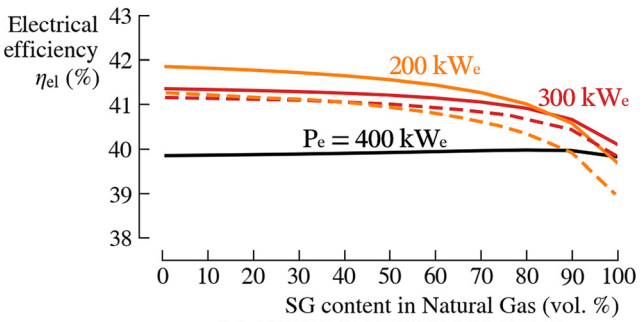

Fig. 7 Electrical efficiency behavior as the volume percentage of syngas increases at two part-load operational schemes (case 1: dashed line, case 2: solid line). The full load performance does not present significant change. 50–100% of syngas decreases the efficiency by 2% at 200 and 300 kW in both cases 1 and 2.

($N_{LP} = N_{HP}$, dashed lines) at part-load, the efficiency at pure natural gas on 300 and 200 kW is almost identical at 41.2% (dashed lines at 0 vol. % SG content) which is also confirmed by Fig. 4. In Fig. 4 we can see that from 310 to 200 kW the efficiency line of case 1 flattens. The performance of case 1 starts to decrease dramatically when the syngas volume percentage exceeds 50% in natural gas (Fig. 7. The efficiency at 300 kW shows 1.3% and at 200 kW 2.31% absolute decrease at 100% syngas. Case 2 ($N_{LP} \neq N_{HP}$, solid lines) presents a higher efficiency at the two part-loads with a variable syngas fraction than case 1. At 300 kW the efficiency of pure syngas even shows an absolute increase of 0.28% and at 200 kW of 0.94%. Furthermore, the efficiency of case 2 does not increase dramatically as we decrease the load in the range of 70–100% of syngas in the fuel mixture. Thus, at high amounts of syngas, the efficiency remains rather constant as the power drops. At the range of 0–70% of syngas, the efficiency increases monotonously as the electric power decreases.

The behavior of the part-load efficiency in cases 1 and 2 is associated with the operating conditions of the LPC. Figure 8 depicts the isentropic efficiency of the LPC ($\eta_{LPC,is}$) of the two cases while we increase the volume percentage of syngas into the fuel. At full load (400 kW) the isentropic efficiency of the component increases as we inject more syngas. This helps the electrical efficiency of the cycle to remain constant (see Fig. 7). The efficiency at 300 kW does not change significantly in both cases and remains almost constant even at high amounts of syngas which is in line with the behavior of electrical efficiency at 300 kW in Fig. 7. At 200 kW the superiority of case 2 is obvious as the isentropic efficiency remains around 83.4% and enhances the total electrical efficiency of the cycle.

At this part of the analysis, it is necessary to also present the LPC map (not only efficiency, as presented before) to get a full picture regarding the behavior of the two-spool mGT when syngas as fuel is used. Figure 9 presents the LPC performance map in normalized values. We can observe that by increasing the volume percentage of syngas, the normalized reduced mass flowrate moves toward the surge line in both control strategies. This can be explained by the difference in fuel LHV. As the LHV of the fuel mixture drops in the syngas case, the demanded fuel flowrate in the CC, to reach the required TIT, increases. However, the flue gas mass flowrate is constant as the LPT is choked. This results in a decrease of the air flowrate of both compressors. In case 2 (solid operating lines) the points of pressure ratio and mass flowrate remain in the region of $\eta_{is}/\eta_{is,des} = 1$ while the dashed lines of case 1 operate at higher pressure ratios. This higher-pressure ratio of the line at 200 kW of case 1 decreases the isentropic efficiency of the component as is also depicted in Fig. 8.

This significant decrease in air flowrate at pure syngas, which is presented in Fig. 9, is linked to a large amount of nitrogen in the fuel (see Table 3). Almost half of the fuel volume is taken by nitrogen which does not take part in the combustion process that gives energy to the flow. As a result, a higher fuel flow rate is needed for the

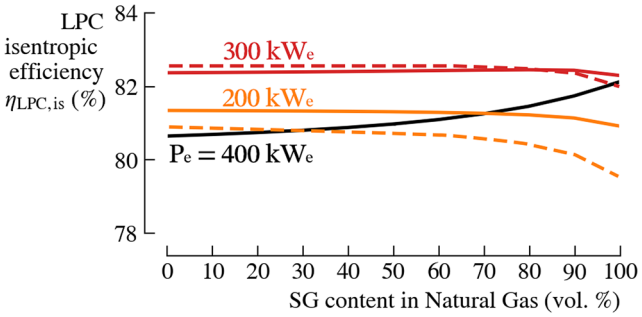

Fig. 8 Isentropic efficiency of LPC at 400, 300, and 200 kW of electric power as the volume percentage of syngas increases in a natural gas—syngas mixture. The efficiency at 200 kW decreases more than 0.3% in case 1 compared to case 2 in the NG–SG mixture.

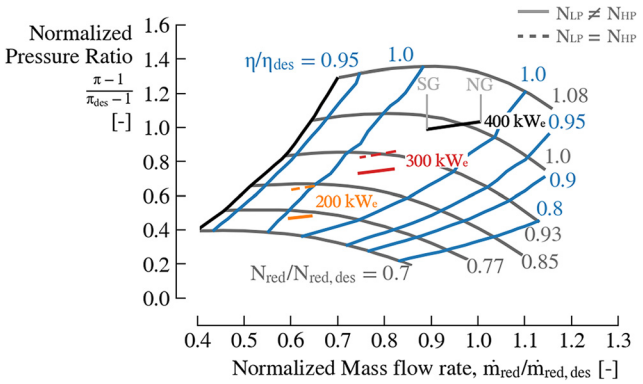

Fig. 9 The behavior of increasing the syngas content in a natural gas—syngas fuel mixture at 3 electric loads (400, 300, 200 kW) depicted in the low-pressure compressor map. The control strategy of case 1 shows higher pressure ratios and lower isentropic efficiencies compared to case 2.

combustion to reach the required TIT. This increased fuel flow rate decreases the air flow rate due to the choking condition on LPT. Thus, the additional normalized airflow rate decrease is 7.3%. Also, the two part-load strategies do not present any significant conclusions on the HPC component. The HPC map presents the operating lines from cases 1 and 2 to be located in the high isentropic efficiency region. Thus, as the HPC isentropic efficiency and also the surge margin remain rather constant, the performance results of HPC in its performance map are not depicted.

As the control scheme of case 1 lets the LPC operate at higher pressure ratios compared to case 2, it is important to calculate from Eq. (2) and evaluate the surge margin behavior in a natural gas—syngas mixture. Figure 10 shows the surge margin (SM), which is calculated from Eq. (2), in the three different generated electric powers. We can see that the SM decreases by 4% from 60 to 100 vol. % of syngas at full-load. However, SM remains over 25% even at 200 kW of case 2 which keeps the LPC at a safe operating region even with high-nitrogen syngas fuel. Although, as the load decreases, case 1 moves the operating points more closely to the surge line. Pure syngas fuel has a surge margin of 22.2% at 300 kW which is considered sufficient, however, at 200 kW the SM goes below 20% with 70 vol. % of syngas. Moreover, at pure syngas, the SM value at 200 kW load is 17%. If the nitrogen amount in syngas increases even more, the safe operation of the mGT is not ensured. We should also consider that the utilized performance maps are obtained using digitization and curve fitting methods. As a result, the current modeling uncertainties lead us to consider that case 1 is not a safe operating strategy at loads below 50% of nominal with pure syngas.

Power Variation at Constant Fuel Composition. In this subsection, different fuel mixtures of natural gas, syngas, and

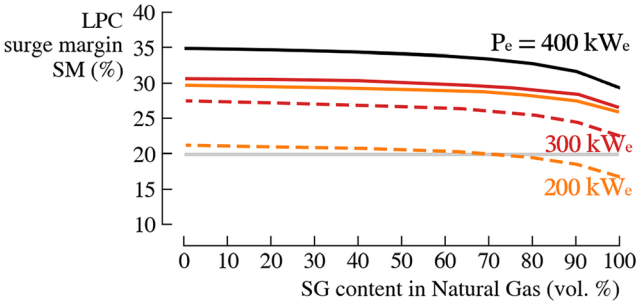

Fig. 10 Low-pressure compressor surge margin at different mixtures of natural gas—syngas. Case 1 (dashed-line) at 200 kW of electric power shows a surge margin below 20% which can lead to operational instabilities.

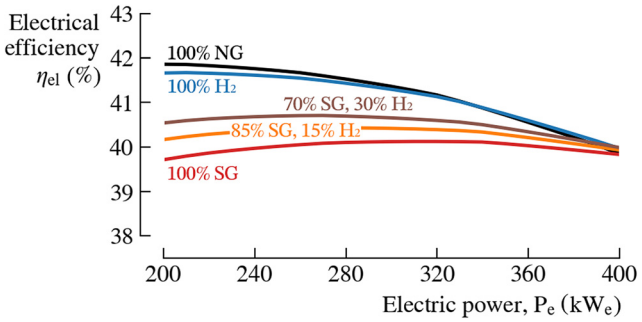

Fig. 11 Electrical efficiency versus electric power of five different fuel mixtures using control strategy case 2. As the hydrogen content in syngas increases (lines: 100% SG, 85% SG 15% H_2, and 70% SG, 30% H_2) the efficiency curve becomes flatter at part-load, and the maximum performance moves toward lower loads.

hydrogen are tested regarding their performance behavior at different loads. Figure 11 presents the electrical efficiency of five different fuel mixtures at an operating range of 200 kW, adopting part-load control strategy case 2. As we discussed in the first paragraph of this chapter, the efficiency curves of pure natural gas (100% NG) and pure hydrogen (100% H_2) are very similar and show the highest electrical efficiency. Only below 280 kW, the two lines start to diverge with slightly higher efficiency for NG. However, the difference remains below 0.2%.

Using syngas lowers the efficiency compared to pure natural gas fuel. One way to compensate, for the lower performance observed with syngas, is the addition of hydrogen to the mixture. As the amount of hydrogen, in a syngas–hydrogen mixture increases (lines red, orange, and brown), the efficiency improves and the maximum value moves toward 200 kW. Furthermore, a 15 vol. % hydrogen addition in the fuel (orange line), increases the efficiency at 200 kW of 0.46%. Also, at 30% of hydrogen (brown line) the efficiency presents almost a constant behavior at the power range of 240 to 320 kW. Therefore, even a 30 vol. % hydrogen addition counteracts the performance disadvantages of syngas consisting of high nitrogen vol. %. This is logical considering the significantly higher LHV of hydrogen compared to syngas.

Conclusions

In this paper, a 0D steady-state model predicted the performance behavior of a two-spool mGT with alternative fuels by applying two different part-load strategies. The model was developed in Python programming language adopting CANTERA object-oriented library to calculate the combustion process effectively. Two different control schemes for the calculation of the part-load operating conditions of the engine are adopted. The first control strategy used identical rotational speeds (case 1). The second strategy was taken from the literature as it is considered to be one of the most efficient for the two-spool mGT (case 2). In that strategy, the rotational speed of the LPS controls the produced power and the shaft speed of the HPS is a function of this generated power using a correlation from the literature. Moreover, the model is compared with another study about a two-spool mGT; temperature and pressure results showed an error below 0.7%.

Three different fuels are utilized for this performance assessment. We observed the performance behavior of the mGT for natural gas, syngas, and hydrogen in the two part-load scenarios (cases 1 and 2). As we add hydrogen to natural gas, the divergence in the operating conditions is insignificant. On the other hand, including syngas in natural gas leads to lower efficiencies. A mixture of natural gas and syngas decreases the air flow rate of the cycle. Pure syngas presents a 7.1% decrease in normalized air flow rate. The nitrogen content mostly influences the air flow rate decrease in LPC toward the surge line. For this reason, hydrogen could be injected into syngas to counteract the efficiency and surge margin decrease. The superiority of control strategy case 2 is highlighted as it presented increased efficiencies at part-load for five different fuel mixtures. Also, control scheme case 1 showed a surge margin below 20% when the amount of syngas is over 70 vol. % in natural gas at 200 kW. This indicates that the LPC could present instabilities in its operation for lower loads and higher nitrogen contents in syngas.

The results show the potential of applying alternative fuels with an effective operational strategy. However, in future work, specific attention should be paid to the calculation of the flame speed of the different fuel mixtures using CFD analysis and chemical kinetics software to determine the occurrence of flashback. Furthermore, a fuel dilution method by injecting water or nitrogen to avoid this phenomenon could be applied.

Acknowledgment

This project has received funding from the European Union's Horizon 2020 research and innovation program under the Marie Sklodowska-Curie grant agreement No 861079 ("NextMGT—Next Generation of Micro Gas Turbines for High Efficiency, Low Emissions, and Fuel Flexibility"). This paper reflects only the authors' view, and the Research Executive Agency and the European Commission are not responsible for any use that may be made of the information it contains.

Funding Data

- Université Catholique de Louvain (Grant No. 86107; Funder ID: 10.13039/501100005041).

Nomenclature

Roman Symbols

c_p = constant pressure heat capacity (kJ/(kg°K))
h = specific enthalpy (J/kg)
K_c = choke constant
$\dot{m}$ = mass flow rate (kg/s)
N = rotational speed (rpm)
p = pressure (Pa)
P = power (kW)
T = temperature (°C)

Greek Symbols

ϵ = heat exchanger effectiveness
η = efficiency (%)
π = pressure ratio

Subscripts

air = properties of air
des = design value
el = electrical
fuel = properties of fuel
int = intercooler
rec = recuperator
red = reduced

Acronyms

CC = combustion chamber
CFD = computational fluid dynamics
CHP = combined heat and power
FAR = fuel-to-air ratio
HPC = high-pressure compressor
HPT = high-pressure turbine
ICE = internal combustion engine
LHV = lower heating value (MJ/kg)
LPC = low-pressure compressor
LPT = low-pressure turbine

mGT = micro gas turbine
mHAT = micro humid air turbine
NG = natural gas
ORC = organic Rankine cycle
PR = pressure ratio
SG = synthesis gas (syngas)
STIG = steam-injected gas turbine
TET = turbine exhaust temperature (°C)
TIT = turbine inlet temperature (°C)

References

[1] Breuhaus, P., Madib, H., Mansouria, M., and Kennedy-Georgec, E., 2021, "An Integrated Energy System to Decarbonise Islands–Gas Turbine Roles and Requirements," 10th International Gas Turbine Conference Gas Turbines in a Carbon-Neutral Society, Virtual, Oct. 11–15, Paper No. 61-IGTC21.
[2] Kolanowski, B. F., 2004, *Guide to Microturbines*, Fairmont Press, Lilburn, GA; New York.
[3] Boukhanouf, R., 2011, *Small Combined Heat and Power (CHP) Systems for Commercial Buildings and Institutions*, Woodhead Publishing, Sawston, CA, pp. 365–394.
[4] Prasad, K., and Jukka, R., 2013, *Generation of Heat and Power From Biogas for Stationary Applications: Boilers, Gas Engines and Turbines, Combined Heat and Power (CHP) Plants and Fuel Cells*, Woodhead Publishing, Sawston, CA, pp. 404–427.
[5] Pilavachi, P. A., 2002, "Mini- and Micro-Turbines for Combined Heat and Power," J. Appl. Therm. Eng., **22**(18), pp. 2003–2014.
[6] Al Moussawi, H., Fardoun, F., and Louahlia, H., 2017, "Selection Based on Differences Between Cogeneration and Trigeneration in Various Prime Mover Technologies," Renewable Sustainable Energy Rev., **74**, pp. 491–511.
[7] Javanshir, A., Sarunac, N., and Razzaghpanah, Z., 2017, "Thermodynamic Analysis of Orc and Its Application for Waste Heat Recovery," Sustainability, **9**(11), p. 1974.
[8] De Paepe, W., Carrero, M. M., Bram, S., Parente, A., and Contino, F., 2014, "Experimental Characterization of a t100 Micro Gas Turbine Converted to Full Humid Air Operation," Energy Procedia, **61**, pp. 2083–2088.
[9] Tiwari, R. N., Reggio, F., Renuke, A., Pascenti, M., Traverso, A., and Ferrari, M. L., 2022, "Performance Investigation of a Bladeless Air Compressor," ASME J. Eng. Gas Turbines Power, **144**(9), p. 091008.
[10] Aurelia Turbines Oy, 2018, "Aurelia - The Most Efficient Small Gas Turbines in the World," Lappeenranta, Finland, accessed Sept. 1, 2024, https://aureliaturbines.com/
[11] Malkamäki, M., Jaatinen-Värri, A., Honkatukia, A., Backman, J., and Larjola, J., 2015, "A High Efficiency Microturbine Concept," 11th European Conference on Turbomachinery Fluid Dynamics & Thermodynamics ETC11, Madrid, Spain, Mar. 23–27.
[12] Jaatinen-Värri, A., Nerg, J., Uusitalo, A., Ghalamchi, B., Uzhegov, N., Smirnov, A., and Malkamäki, M., 2016, "Design of a 400 kw Gas Turbine Prototype," ASME Paper No. GT2016-56444.
[13] Mansouri, M., Madi, H., and Breuhaus, P., 2022, "Establishment of a Baseline Integrated Energy System to Decarbonise Geographical Islands," ASME Paper No. GT2022-82918.
[14] Shih, H.-Y., and Liu, C.-R., 2014, "A Computational Study on the Combustion of Hydrogen/Methane Blended Fuels for a Micro Gas Turbines," Int. J. Hydrogen Energy, **39**(27), pp. 15103–15115.
[15] Rajpara, P., Shah, R., and Banerjee, J., 2018, "Effect of Hydrogen Addition on Combustion and Emission Characteristics of Methane Fuelled Upward Swirl Can Combustor," Int. J. Hydrogen Energy, **43**(36), pp. 17505–17519.
[16] Cappelletti, A., and Martelli, F., 2017, "Investigation of a Pure Hydrogen Fueled Gas Turbine Burner," Int. J. Hydrogen Energy, **42**(15), pp. 10513–10523.
[17] Pappa, A., Bricteux, L., Bénard, P., and De Paepe, W., 2021, "Can Water Dilution Avoid Flashback on a Hydrogen-Enriched Micro-Gas Turbine Combustion–A Large Eddy Simulations Study," ASME J. Eng. Gas Turbines Power, **143**(4), p. 041008.
[18] Bompas, J., and De Paepe, W., 2021, "Fuel Flexibility of a 100kwe Micro Gas Turbine: Combustion Performance Using Natural Gas and Non-Conventional Syngas," International Conference on Applied Energy, Thailand/Virtual, Nov. 29–Dec. 5, Paper No. 487.
[19] Diaz, R., Ochoa, G. V., and Peralta, Y., 2018, "Exergoeconomic Analysis of a Syngas Micro Turbine Cogeneration System," Chem. Eng. Trans., **65**, pp. 655–660.
[20] Reale, F., Sannino, R., Calabria, R., and Massoli, P., 2020, "Numerical Study of a Small-Scale Micro Gas Turbine-Orc Power Plant Integrated With a Biomass Gasifier," ASME Paper No. GT2020-15401.
[21] Renzi, M., Patuzzi, F., and Baratieri, M., 2017, "Syngas Feed of Micro Gas Turbines With Steam Injection: Effects on Performance, Combustion and Pollutants Formation," Appl. Energy, **206**, pp. 697–707.
[22] De Paepe, W., Renzi, M., Carrerro, M. M., Caligiuri, C., and Contino, F., 2019, "Micro Gas Turbine Cycle Humidification for Increased Flexibility: Numerical and Experimental Validation of Different Steam Injection Models," ASME J. Eng. Gas Turbines Power, **141**(2), p. 021009.
[23] Jaatinen-Värri, A., Backman, J., Honkatukia, J., and Malkamäki, M., 2017, "A Comparison of Small-Scale Gas Turbine Control Schemes," ASME Paper No. GT2017-64329.
[24] Gaitanis, A., Contino, F., and De Paepe, W., 2023, "Real Time Micro Gas Turbines Performance Assessment Tool: Comprehensive Transient Behavior Prediction With Computationally Effective Techniques," ASME J. Eng. Gas Turbines Power, **145**(3), p. 031006.
[25] Bell, I. H., Wronski, J., Quoilin, S., and Lemort, V., 2014, "Pure and Pseudo-Pure Fluid Thermophysical Property Evaluation and the Open-Source Thermophysical Property Library Coolprop," Ind. Eng. Chem. Res., **53**(6), pp. 2498–2508.
[26] Wagner, W., and Pruß, A., 2002, "The Iapws Formulation 1995 for the Thermodynamic Properties of Ordinary Water Substance for General and Scientific Use," J. Phys. Chem. Ref. Data, **31**(2), pp. 387–535.
[27] Virtanen, P., Gommers, R., Oliphant, T. E., Haberland, M., Reddy, T., Cournapeau, D., Burovski, E., et al., 2020, "SciPy 1.0: Fundamental Algorithms for Scientific Computing in Python," Nat. Methods, **17**(3), pp. 261–272.
[28] Cengel, Y. A., and Boles, M. A., 2006, *Thermodynamics: An Engineering Approach*, McGraw-Hill, New York.
[29] Parente, J., Traverso, A., and Massardo, A., 2003, "Micro Humid Air Cycle: Part A—Thermodynamic and Technical Aspects," ASME Paper No. GT2003-38326.
[30] Endowers Solutions Pvt. Ltd., 2021, "Endowers Solutions Private Limited," Maharashtra, India, accessed Nov. 9, 2022, https://www.endowers.in/
[31] Goodwin, D. G., Moffat, H. K., Schoegl, I., Speth, R., and Weber, B. W., 2023, "Cantera: An Object-Oriented Software Toolkit for Chemical Kinetics, Thermodynamics, and Transport Processes," Version 3.0.0.
[32] Montagnaro, F., and Zaccariello, L., 2022, "Gasification of Spruce Wood Chips in a 1.5 Mwth Fluidised Bed Reactor," Energies, **15**(16), p. 5883.
[33] El-Nagar, R. A., and Ghanem, A. A., 2019, *Syngas Production, Properties, and Its Importance*, Vol. 2, Intech Open, London, UK.
[34] Bandara, J., Jaiswal, R., Nielsen, H., Moldestad, B., and Eikeland, M., 2021, "Air Gasification of Wood Chips, Wood Pellets and Grass Pellets in a Bubbling Fluidized Bed Reactor," Energy, **233**, p. 121149.
[35] Lalsare, A., Wang, Y., Li, Q., Sivri, A., Vukmanovich, R. J., Dumitrescu, C. E., and Hu, J., 2019, "Hydrogen-Rich Syngas Production Through Synergistic Methane-Activated Catalytic Biomass Gasification," ACS Sustainable Chem. Eng., **7**(19), pp. 16060–16071.